COMPUTATIONAL ELECTROMAGNETIC MODELLING OF NEAR-FIELD ANTENNA TEST SYSTEMS USING PLANE WAVE SPECTRUM SCATTERING MATRIX APPROACH

A.C. Newell, S.F. Gregson
Nearfield Systems Inc.
19730 Magellan Drive
Torrance, CA, 90502 USA

ABSTRACT

In recent years a number of analyses and simulations have been published that estimate the effect of using a probe with higher order azimuthal modes with standard probe corrected spherical transformation software. In the event the probe has higher order modes, errors will be present within the calculated antenna under test (AUT) spherical mode coefficients and the resulting asymptotic far-field parameters [1, 2, 3, 4]. Within those studies, a computational electromagnetic (CEM) simulation tool was developed to calculate the output response for an arbitrary AUT/probe combination where the probe could be placed at arbitrary locations on the measurement sphere ultimately allowing complete near-field acquisitions to be simulated. The planar transmission equation was used to calculate the probe response using the plane wave spectra for actual AUTs and probes derived from either planar or spherical measurements. The planar transmission formula was utilised as, unlike the spherical analogue, there is no limitation on the characteristics of the AUT or probe thereby enabling a powerful, entirely general, model to be constructed. This paper further extends this model to enable other measurement configurations and errors to be considered including probe positioning errors which can result in ideal first order probes exhibiting higher order azimuthal mode structures. The results of these additional simulations are presented and discussed.

Keywords: near-field, antenna measurements, near-field probe, spherical alignment, spherical mode analysis.

1.0 Introduction

This paper extends previous studies in which the effect of the presences of higher order azimuthal probe spherical mode coefficients when the classical spherical numerical software which uses mode orthogonality to solve for the spherical mode coefficients (SMC) of the antenna under test (AUT) is employed [1, 2, 3, 4]. In this commonly used spherical near-field to far-field transform approach, the probe is assumed to have only modes for which $\mu = \pm 1$ with all higher order azimuthal spherical mode coefficients being assumed to be identically zero. In the event the probe has non-zero higher order azimuthal modes, as is often the case in practice, errors will be present within the calculated AUT spherical coefficients and the corresponding asymptotic far-field data. In those previous studies, a novel computational electromagnetic (CEM) simulation was developed to calculate the output response for an arbitrary AUT/probe combination where the probe could be placed at arbitrary locations in the near-field. The planar transmission equation was used to calculate the probe response using the plane wave spectrum method for actual AUTs and probes derived from either planar or spherical near-field measurements. The planar transmission formula was utilized as there is no inherent limitation on the characteristics of the AUT or probe thereby allowing a very general model to be constructed. The positions and orientations of the AUT and probe were specified using a combination of isometric rotations of the antenna's spectra and the x, y, z position of the probe used in the transmission equation. The simulation was carried out for rectangular open ended waveguide (OEWG) probes using all of the higher order modes and also for the same probe where only the $\mu = \pm 1$ modes were present to calculate the probe patterns.

During those simulations the far-field difference level was computed and found to be primarily in the main beam region and at a level 40 to 60 dB below main beam peak for measurement radii of one and four times the maximum radial extent (MRE) respectively. Thus, the initial conclusion was that the effect of the higher order modes on typical measurements using OEWG probes would be smaller than other commonly encountered measurement errors and therefore have little practical effect on the far-field results. The results of those simulations were presented and guidelines developed to aid in the choice of spherical near-field probes and measurement radii for typical antennas [3, 4]. However, within those simulations it was assumed that the spherical system being modelled was perfectly aligned with the probes being rotated coaxially about the longitudinal axis of the waveguide section. It is well known from standard spherical near-field sampling theory that displacing a

source away from the measurement origin has the effect of exciting progressively higher order modes [5]. Thus, it is possible, as a consequence of imperfections in the alignment, or characterization, of the near-field probe, that even a "perfect" first order probe can exhibit significant non-first order behavior. This mechanical configuration is illustrated below in Figure 1 where the observer is looking into the aperture of an OEWG probe which is shown in two χ, *i.e.* polarization, positions (0° and 90°) and has been translated in the *x*- and *y*-axes by an amount Δx and Δy respectively.

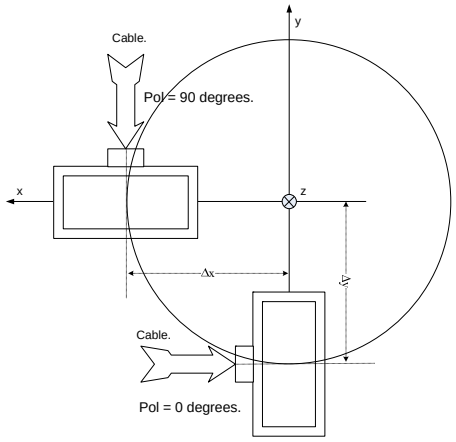

Figure 1: Schematic of spherical measurement system showing probe axis alignment error. Here probe translation from χ = 0° position to χ = 90° position is shown.

It can be shown that the general form of the far-field pattern of a rotational symmetrical first order probe satisfies the equation [6],

$$\underline{K}(\theta,\phi) = \left[K_\theta(\theta,\phi=0°)\cos\phi + K_\theta(\theta,\phi=90°)\sin\phi\right]\underline{\hat{e}}_\theta + \left[K_\phi(\theta,\phi=0°)\cos\phi + K_\phi(\theta,\phi=90°)\sin\phi\right]\underline{\hat{e}}_\phi \quad (1)$$

Where for the $\mu = \pm 1$ rotational symmetry to hold it is *also* necessary for the probe to be symmetrical in θ, thus only the conventional, or first, sphere data is used to generate the probe patterns, or alternatively only the alternate, or second, sphere is used [7]. Thus, the complete pattern can be determined from the far-field cardinal cuts. From the shifting property of the Fourier transform, it is possible to show that the pattern of a translated antenna can be obtained by applying a differential phase change [8]. Thus, a probe that has been translated in the *x*- and/or *y*-axis can be obtained from a nominally aligned probe through,

$$\underline{K}_t(\theta,\phi) = \underline{K}(\theta,\phi)e^{-jk_0(u\Delta x + v\Delta y)} \quad (2)$$

Here, k_0 is the free-space propagation constant, and *u* & *v* are the conventional Cartesian direction cosines that are related to the polar spherical angles through, $u = \sin\theta\cos\phi$, $v = \sin\theta\sin\phi$. To illustrate the effect that this has on the corresponding probe SMCs, Figure 2 presents the $s = 1$, *i.e.* transverse electric (TE), SMCs for a perfectly aligned first order probe. In this case, the first order probe corresponds to an open ended rectangular waveguide (WR90) probe with all the higher order azimuthal modes having first been filtered out by taking the far-field cardinal pattern cuts and reconstructing the complete far-field pattern using equation (1). Here, the SMC are presented in the form of a false colour checkerboard plot of the amplitude of the SMCs. The white space denotes mode coefficients for combinations of *M* and *N* that do not have a physical significance. Conversely Figure 3 presents the same data in an alternative form. Here, the amplitude mode spectrum corresponding to $s = 1$, $M = 0, 1, 2, 3, 4$, and 5 SMCs, are plotted as a function of the *N* index. From inspection of these plots, it is evident that for a perfectly aligned first order probe, the SMC amplitudes are zero for all modes where $M \neq |1|$ thereby providing verification of the correct application of equation (1). Figure 4 contains an equivalent false-colour plot for the case where the probe has been displaced from the origin by 0.1 wavelengths in the *x*-axis, and Figure 6 contains an equivalent plot only here the displacement has been increased to 0.2 wavelengths.

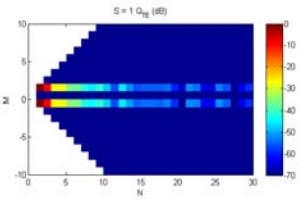

Figure 2: False colour plot of SMCs of correctly aligned first-order probe

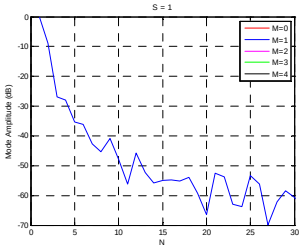

Figure 3: Plot of SMCs of correctly aligned first-order probe

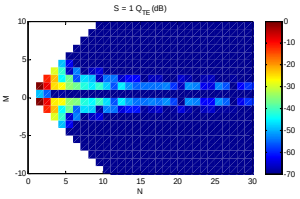

Figure 4: False colour plot of SMCs of first order probe offset by 0.1λ in *x*-axis

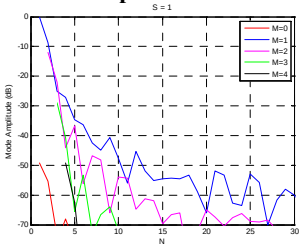

Figure 5: Plot of SMCs of first order probe offset by 0.1λ in *x*-axis.

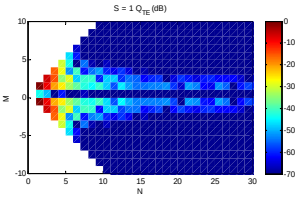

Figure 6: False colour plot of SMCs of first order probe offset by 0.2λ in *x*-axis

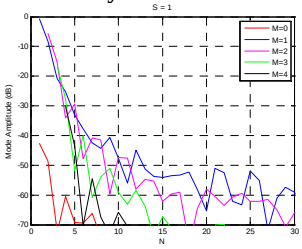

Figure 7: SMCs of first order probe offset by 0.2λ in *x*-axis.

Figures 5 and 7 contain mode plots that are equivalent to those shown within Figure 3 which clearly illustrate the increase in power that is contained within the higher order azimuthal mode coefficients that results from increasingly large tangential probe translations. It is worth reiterating at this point that *all* of these mode spectra were obtained from the same rotationally symmetrical first order probe with a mathematical displacement being applied using equation (2). Here, the SMCs were computed using standard spherical near-field processing [1, 6]. These plots illustrate the general behavior which is that progressively higher order azimuthal modes are excited as the probe offset in the *x*- or *y*-axes increases with this being true irrespective of the type or design of probe being considered. Displacement in the *z*-axis results in higher order polar modes being excited however this does not invalidate the $\mu = \pm 1$ constraint.

2.0 Overview of Simulation Technique

The novel plane wave spectrum based simulation technique has been described in detail in previous papers [1, 2] and will only be summarized here. Previously measured spherical near-field data for both the AUT and a probe is used to calculate the far-field patterns of both antennas over a full sphere. The AUT far-field pattern is then rotated mathematically about the *z*-axis to simulate a ϕ-rotation and about the *y*-axis to simulate a θ-rotation. The transmitting plane wave spectrum over the forward hemisphere on a *k*-space grid is then derived from the rotated pattern. This plane-wave spectrum represents the AUT rotated in (θ,ϕ) as it is in a conventional spherical near-field measurement. Specifying a *z*-offset when calculating the AUT far-field pattern allows the radius of the simulated measurement to be controlled. So as to generalize the simulation as far as possible, the simulated measurement radius was specified as a multiple of the maximum radial extent (MRE) of the AUT thereby allowing generalization of the results to other probe/AUT combinations. In this case a high gain *x*-band slotted waveguide array antenna was used, as shown in Figure 8, which had a conceptual MRE of 18" (0.46 m).

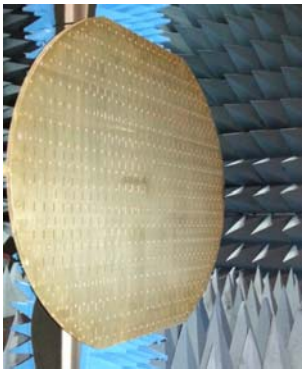

Figure 8: x-band slotted waveguide planar array antenna used as the AUT within the SNF simulations.

The plane wave spectrum of the probe is also rotated about the *z*-axis of the probe by the angles $\chi = 0$ *and* $\chi = 90$ to simulate the two probe rotations of a standard spherical near-field measurement and its receiving plane wave spectrum calculated on the same *k*-space grid as was used to tabulate the AUT. The AUT and probe plane wave spectra are combined using the standard transmission formula, which corresponds to convolving the two pattern functions in the near-field, and then integrated to compute the simulated measurement for a single (r, θ, ϕ, χ) point. That is to say, an inverse two-dimensional Fourier transform is performed to reconstruct the radiated near-fields. The calculation of a receiving plane-wave spectrum for the OEWG probe is repeated but in this case, the offset probe pattern is used and the convolution/integration is repeated. This provides two simulated measurement points represent, respectively, a spherical near-field sample using a first order probe, and a higher order *x*- or *y*-axis translated probe with otherwise identical patterns and polarization properties. The simulation technique as implemented omits reactive fields as non-visible spectra are filtered out prior to integrating. However, actual spherical near-field measurements are also taken outside of this region of space and this limitation is therefore of no practical concern. Also, multiple reflections between the probe and the AUT are omitted from the simulation however these too are omitted from all standard near-field theories.

A more efficient processing technique was introduced within an earlier paper [4] which roughly halved the simulation times, and in this study that gives additional insight into the effect of the higher order modes by modeling a general probe as the sum of an ideal probe with only the first order modes and a fictitious *difference* probe that contains only the higher order modes. That is to say,

$$\vec{s}'_{02}(\vec{K},\chi) = \vec{s}'_{02F}(\vec{K},\chi) + \Delta_{02H}(\vec{K},\chi)$$

where

$\vec{s}'_{02F}(\vec{K},\chi)$ = Ideal first order probe using $\mu = \pm 1$ modes of actual probe.

$\Delta_{02H}(\vec{K},\chi)$ = Higher order probe using $\mu \neq \pm 1$ modes of actual probe. (3)

The far-field pattern and therefore the receiving plane wave spectrum for the difference probe can be calculated by the spherical software using the measured probe near-field data while setting the first order modes to zero when the far-field is calculated. The error in the near-field data due to the higher order modes can be calculated directly in a single step by using only the difference probe spectrum in the transmission equation. The far-field error can then be calculated by processing this difference probe near-field data using the standard spherical software.

3.0 Summary of Results

Utilizing the concept of a difference probe, the θ and ϕ polarized difference spectra for the case where the probe has been offset in *x* by 0.1λ are shown in Figures 9 & 10.

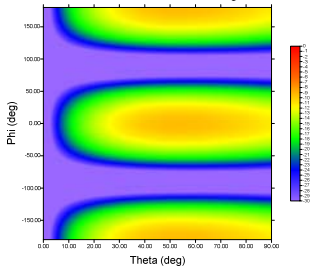

Figure 9: θ-component pattern for OEWG probe with 0.10 λ offset in *x*.

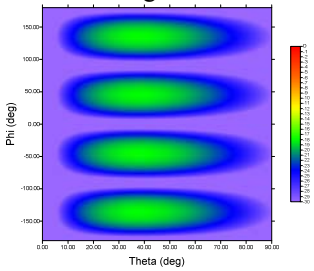

Figure 10: ϕ-component pattern for OEWG probe with 0.10 λ offset in *x*.

Here, the amplitudes are plotted relative to the peak of the first order probe pattern. The error in the simulated near-field is given by the convolution of the difference probe spectrum and the AUT transmitting spectrum which are shown in Figures 11 and 12.

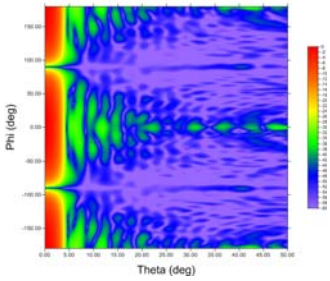

Figure 11: θ-component far-field pattern for slotted array AUT.

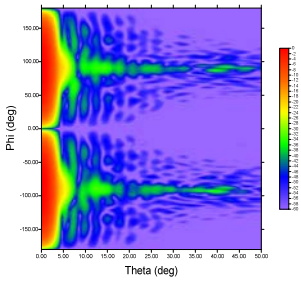

Figure 12: ϕ-component far-field pattern for slotted array AUT.

The amplitude of the complex difference is shown in Figures 13 and 14 where the complex difference is defined as follows,

$$\Delta_{\text{complex}} = 20\log_{10}\left(\left|E_1 - E_2\right|\right) \qquad (4)$$

Here, E_1 and E_2 denote the spherical field components being compared. This definition of adjacency takes into account phase differences that are crucial when

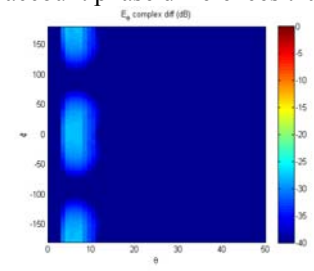

Figure 13: Difference amplitude peak = -27.5 dB) near-field pattern for Δx=0.1λ and measurement radius = 4×MRE.

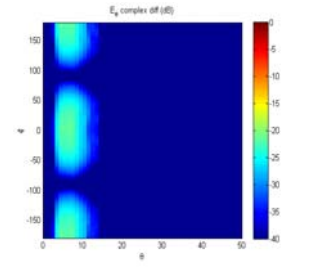

Figure 14: Difference amplitude (peak = -21.6 dB) near-field pattern for Δx=0.2λ and measurement radius = 4×MRE.

In Figure 15, the near-field errors are plotted for specific (θ,ϕ,χ) points as a function of measurement radius. This type of plot illustrates the character of the near-field error versus measurement radius where the specific points here are near the peaks (θ = 10° and 5°) and nulls (θ = 0°) of the error patterns at a fixed distance shown in Figures 13 and 14.

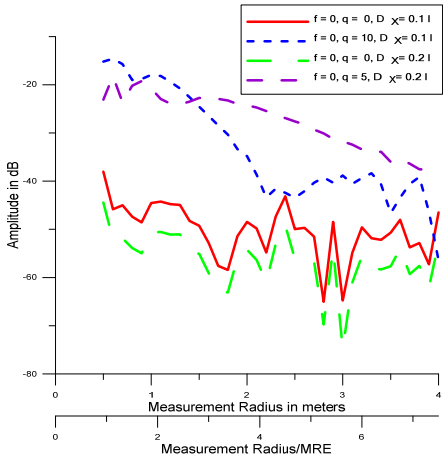

Figure 15: Near-field complex error difference versus measurement radius.

examining near-field data is subsequently transformed to the far-field.

Since the AUT pattern is focused with the highest amplitudes near θ = 0° and the difference probe has a null in this region, *c.f.* Figures 9 and 10 above, the error caused by the higher order modes is very low in the AUT boresight direction. The near-field error pattern is therefore localized to a region slightly off boresight where the sidelobes of the AUT couple with the peak of the difference probe pattern. Clearly, the near-field data can be transformed to the far-field using standard spherical near-field processing. Figure 16 below contains a comparison of the far-field antenna pattern as obtained using an ideally orientated probe, which are denoted with red contours, and an identical probe that has been offset by 0.1λ in the *x*-axis, which are denoted by black contours. Here, the contours are plotted -50 -40 -30 -20 -10 -5 -3 -2 -1 dB levels below the peak of the pattern.

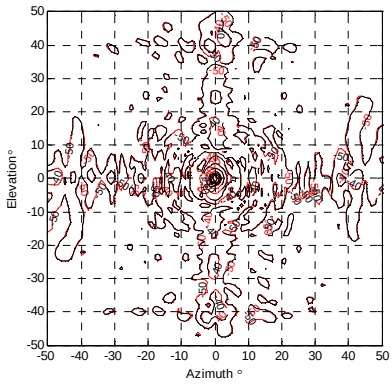

Figure 16 Red denotes reference far-field pattern, black denotes 0.1λ *x*-axis offset probe at a measurement radius of 4×MRE.

As the degree of agreement attained between the respective far-field patterns is very encouraging, equivalent difference plots can again be produced to quantify the behavior and similarities. In the far-field, conventional amplitude difference plots can be employed as the phase comparison is far less crucial in this region. Again, the differences are most significant in the main beam region and fall off to very low levels elsewhere with the degree of agreement improving as the measurement radii increases.

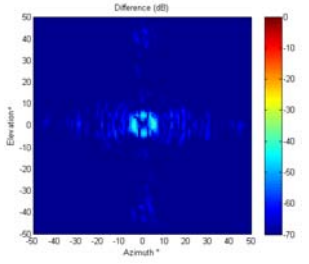

Figure 16: amplitude difference far-field pattern for $\Delta x = 0.1\lambda$ and measurement radius = 4×MRE.

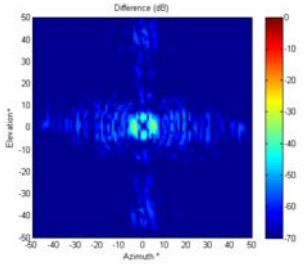

Figure 17: amplitude difference far-field pattern for $\Delta x = 0.2\lambda$ and measurement radius = 4×MRE.

5.0 Summary and Conclusions

The results presented above are broadly similar to those reported within previous studies that focused on the use of OEWG probes with standard SNF processing. At the minimum measurement radius (2×MRE) with a 0.1 λ *x*-axis offset, there are points in the near-field where the complex amplitude errors due to the higher order modes are only 22 dB below the correct values and this is high enough that it could be observed in an actual measurement. However, and as has been the case with other higher order azimuthal mode related errors, the complex amplitude differences reduce as the radius increases. Here, the complex difference reduced to 27 dB below the correct values when the radius doubled to 4×MRE. The effect on the far-field pattern is primarily on the main beam region and the sidelobes have very small errors. The peak main beam errors for the 2×MRE simulations with 0.1λ *x*-axis peak positional error are on the order of 34 dB below the main beam peak which may not be acceptable for high accuracy measurements. However, this peak level can be reduced by using measurement radii greater than this and at 4×MRE the error level reduced to 40 dB. Furthermore, the graphical results presented above can be used to determine the required distance for a desired accuracy level. The effect of the misalignment was found to decrease with distance which agreed with practical experience and is an additional indication of reliability of the simulations. Furthermore, by comparing and contrasting the results as summarized above, with those of the previous studies [1, 2, 3, 4] it is apparent that excitation of higher order azimuthal SMC as a result of imperfections within probe alignment are potentially a larger component within the facility level uncertainty budget than using a rectangular OEWG probe in place of a true first order rotationally symmetrical probe.

The use of the planar transmission equation and plane wave spectrum technique to simulate near-field data on a spherical surface, and potentially other surfaces, has been demonstrated and shown to be a powerful tool for analysing near-field measurements. Independent algorithms using different software were developed by the two authors and the very close agreement attained between in the results substantiates the method and the implementations. Again, the complex differences in the near-field were found to provide a good predictor of the far-field differences, thus simulations at representative angles can be used to analyze other AUT/probe/frequency combinations without the need to produce complete full near-field simulations and compare the transformed far-fields with the difference levels being generally insensitive to the AUT characteristics.

REFERENCES

[1] A.C. Newell, S.F. Gregson, "Estimating the Effect of Higher Order Modes in Spherical Near-Field Probe Correction", Antenna Measurement Techniques Association (AMTA) 34th Annual Meeting & Symposium, Bellevue, Washington October 21-26, 2012.

[2] A.C. Newell, S.F. Gregson, "Higher Order Mode Probes in Spherical Near-Field Measurements", 7th European Conference on Antennas and Propagation (EuCAP 2013) 8-12 April 2013.

[3] A.C. Newell, S.F. Gregson, "Estimating the Effect of Higher Order Modes in Spherical Near-Field Probe Correction", Antenna Measurement Techniques Association (AMTA) 35th Annual Meeting & Symposium, Columbus, Ohio, October 6-11, 2013.

[4] A.C. Newell, S.F. Gregson, "Estimating the Effect of Higher Order Azimuthal Modes in Spherical Near-Field Probe Correction", The 8th European Conference on Antennas and Propagation (EuCAP 2014) 6-11 April 2014.

[5] T.A. Laitinen, S. Pivnenko, and O. Breinbjerg, "Theory and Practice of the FFT/Matrix Inversion Technique for Probe-Corrected Spherical Near-Field Antenna Measurements With High-Order Probes" IEEE Trans. Antennas Propag., vol. 58, No. 8, pp. 2623–2631, August 2010.

[6] J.E. Hanson, Ed., "Spherical Near-Field Antenna Measurements", IEE Electromagnetic Waves Series 26, 1988, Peter Peregrinus Ltd, London, UK, ISBN 0 86341 110 X, pp. 149.

[7] G.F. Masters, S.F. Gregson, "Co-ordinate System Plotting for Antenna Measurements", Antenna Measurement Techniques Association (AMTA) Annual Meeting & Symposium 2007 St Louis Missouri.